Journal of Computational Electronics (2024) 23:931–944
https://doi.org/10.1007/s10825-024-02192-3

A computational investigation on the adsorption behavior of bromoacetone on B_{36} borophene nanosheets

Meriem Taier[1,7] · Hamza Allal[2,3] · Salim Bousba[2,4] · Fathi Bouhadiouche[1,7] · Soumeya Maza[2,5] · Maamar Damous[1,2] · Ahlem Boussadia[2,6]

Received: 2 January 2024 / Accepted: 13 June 2024 / Published online: 26 June 2024

Abstract

Density functional theory (DFT) methods are employed to investigate the capability of B_{36} borophene nanosheets as sensors for detecting the bromoacetone (BCT) molecule. An evaluation of the structural and electronic properties of both BCT and B_{36} borophene is conducted. Subsequently, through computed metrics such as adsorption energy, charge density difference, and density of states, the interaction between B_{36} and the BCT molecule is examined via dispersion-corrected density functional theory (DFT). Employing the reduced density gradient approach for the analysis of non-covalent interactions, we further explored the nature of these interactions. The obtained results illustrate that B_{36} borophene nanosheets serve as effective sensors for the BCT molecule, showcasing their ability to adsorb up to five BCT molecules through an exothermic process. BCT molecules chemiadsorb onto B_{36} borophene by forming B−O covalent bonds, engaging the oxygen atom of the carbonyl group in BCT with the edge boron atoms of B_{36} borophene. Additionally, BCT molecules physio-adsorb on both the concave and convex sides of B_{36} borophene, facilitated by van der Waals interactions. Ab-initio molecular dynamic simulations confirm the thermal stability of the BCT@B_{36} concave and convex complexes at both 300 K and 400 K.

Keywords DFT · B_{36} borophene · Boromoacetone · Sensor · Adsorption

1 Introduction

Harmful and hazardous substances may infiltrate the environment through various routes, including industrial emissions, agricultural runoff, and the use of consumer products [1–3]. These compounds possess the potential to pose risks to human health and the environment, leading to issues such as cancer, birth defects, neurological damage, and other health concerns [4, 5]. The removal of toxic and hazardous substances from the environment involves a range of procedures and approaches aimed at reducing or eliminating pollutants that pose threats to ecosystems and human well-being.

Adsorption is one of the techniques used to remove poisonous and dangerous chemicals from various mediums like air and water [6–10]. This method involves the adhesion of these substances (adsorbate) to the surface of a solid material (adsorbent), which could be activated carbon [11], zeolites [12], silica gel [13], clay minerals [14–16], activated alumina [17], molecular sieves [18], graphene and carbon nanotubes [19], germanene [20], or other specifically designed materials. Nevertheless, owing to their distinctive

✉ Hamza Allal
hamzaallal.univ@gmail.com

1 Faculty of Technology, 20 August 1955 University of Skikda, El Hadaik Road, P.O. Box 26, Skikda, Algeria

2 Research Unit of Environmental Chemistry and Molecular Structural (CHEMS), University of Constantine 1 (Mentouri), Constantine, Algeria

3 Department of Process Engineering, Faculty of Process Engineering, University of Salah Boubnider Constantine 3, Constantine, Algeria

4 Laboratoire de Recherche Sur le Médicament et le Développement Durable «ReMeDD», Université Salah Boubnider Constantine 3, Constantine, Algeria

5 Department of Chemistry, Faculty of Exact Sciences, University of Constantine 1 (Mentouri), Constantine, Algeria

6 Ecole Nationale Supérieure de Biotechnologie Taoufik Khaznadar (ENSB), ville Universitaire Ali Mendjli, Constantine 3, Constantine, Algeria

7 LRPCSI-Laboratoire de Recherche sur la Physico-Chimie des Surfaces et Interfaces, Université 20 Août 1955, Skikda, Algeria

characteristics at the nanoscale, 2D materials, including borophene (frequently allocated to a graphene cousin), have garnered attention for their potential applications as adsorbents. The borophene B_{36} nanosheet, a specific variant of 2D material comprising a single layer of boron atoms, is frequently employed as an adsorbent for toxic and hazardous substances [21–29]. This preference is attributed to its expansive surface area, high porosity, and exceptional chemical reactivity.

Density functional theory (DFT) computations and ab-initio molecular dynamics (MD) simulations represent computational tools employed to investigate the adsorption behavior of small compounds on adsorbent materials. DFT methods help analyze the electronic structure of both the adsorbate and adsorbent molecules, as well as their interactions (interaction between adsorbate and adsorbent) at an atomic level [29–31]. Meanwhile, ab-initio molecular dynamic (MD) simulations provide a comprehensive examination of the dynamic behavior of these complexes (adsorbate–adsorbent) over time and at different temperatures [32–35].

During the last decade, several researchers [21–29] have focused their efforts on examining and understanding the mechanisms of interaction between some extremely toxic chemicals and B_{36} borophene nanosheet using the density functional theory (DFT) methods. Kootenaei et al. [21] explored the reactivity and electronic sensitivity of B_{36} borophene toward HCOH gas. Their findings suggest that the concentration of HCOH gas notably impacts borophene conductance, indicating that an increase in the quantity of HCOH molecules leads to a corresponding elevation in conductance.

Mohsenpour and co-workers [22] employed density functional theory (DFT) calculations to explore the potential of the B_{36} nanosheet as a chemical sensor for the detection of pollutants such as formaldehyde, acetaldehyde, and propanal. The results show that boron atoms on the edges of the nanosheet are more reactive than those in the interior and that the number of adsorbed pollutant molecules affects both the adsorption energy and the electronic properties of the B_{36} nanosheet.

Li and Zhao [27] investigated the interactions between mercaptopurine and B_{36} using the DFT method. The observations indicated that the boron atoms positioned at the edges of B_{36} nanosheets exhibited higher reactivity compared to the internal boron atoms when interacting with mercaptopurine (MP). Furthermore, their conclusion underscored the pronounced tendency of MP molecules to be adsorbed, particularly via their nitrogen heads, onto the edges of B_{36}.

Allal and all co-workers [29] conducted a computational analysis using DFT to investigate the borophene B_{36} nanosheet's potential as a sensor for the harmful acrolein molecule. The results corroborated previous literature [21–29], confirming the borophene B_{36} nanosheet's suitability as a highly promising candidate for detecting and removing acrolein molecules.

On the other hand, bromoacetone CH_3COCH_2Br (see Fig. 1) is an exceedingly toxic chemical recognized for inducing severe irritation, burns, and tissue damage upon contact with the skin, eyes, or respiratory system [36, 37]. Its strong irritating qualities are highlighted by its historical employment as a lachrymatory weapon in chemical warfare. Because of this molecule's hazardous nature and detrimental effects on both human health and the environment, handling and regulation of it are imperative. Exposure to this compound may cause skin irritation, eye damage, and respiratory difficulties.

In this study, we examined the electronic structures of the bromoacetone (BCT) molecule and the borophene B_{36} nanosheet. Our investigation focused primarily on assessing the potential of the B_{36} nanosheet as a chemical sensor for the BCT molecule, employing ab-initio molecular dynamic (AIMD) simulations and density functional theory (DFT) calculations.

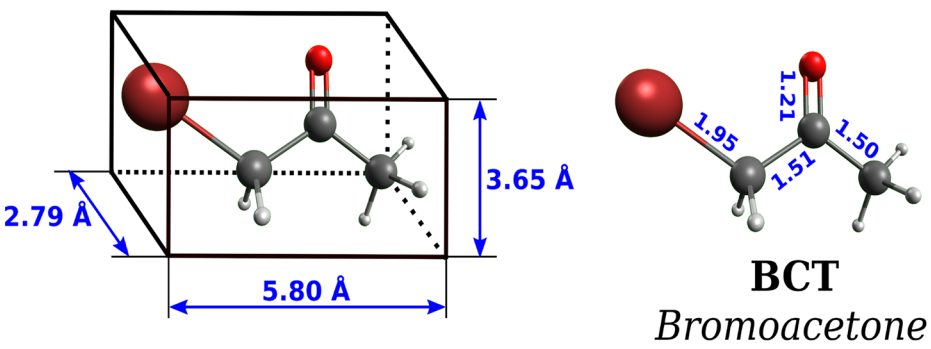

Fig. 1 Optimized structure of the BCT molecule

2 Computational details

2.1 Quantum chemical calculations

All geometry optimizations in this study were carried out using ORCA program package (version 5.0.0 and 5.0.4) [38]. Firstly, the isolated electronic structures of BCT and B_{36} have been optimized at B3LYP-D3/def2-TZVPP [39, 40] of level theory, and then after, several configurations of interactions between BCT and B_{36} were investigated and analyzed. Different functionals of the Head-Gordon group [41] were also performed such as B97M, ωB97X, and ωB97M [42] in combination with the D4 dispersion correction, and using the modified triple-ζ basis sets def2-mTZVP [43]. Further, in order to predict and compare behavior of interaction between BCT and B_{36}, we include the recent r2SCAN-3c composite method [44], based on the r2SCAN [45, 46] meta-GGA combined with the D4 dispersion correction [47] and geometrical counter poise-correction [48].

The molecular electrostatic potential (MEP) [49] was performed by ORCA package and visualized using the UCSF Chimera program (version 1.10.2) [50]. Reduced density gradient (RDG) and density of state (DOS) analyses were adopted by Multiwfn program [51]. However, Fukui function isosurface plots (electrophilic (f^-) and nucleophilic (f^+)) were visualized by VMD program [52] based on the cube files generated by Multiwfn software.

The conceptual DFT-based global and local reactivity descriptors were estimated to predict the reactivity and reactive sites on the BCT and B_{36} molecules. The global reactivity descriptors such as highest occupied molecular orbital ($\mathbf{E_{HOMO}}$) and the lowest unoccupied molecular orbital ($\mathbf{E_{LUMO}}$), energy gap ($\mathbf{\Delta E_{gap}}$), global hardness ($\boldsymbol{\eta}$), global softness ($\boldsymbol{\sigma}$), global electrophilicity ($\boldsymbol{\omega}$), electro-donating power ($\boldsymbol{\omega^-}$), electro-accepting power (ω^+), net electrophilicity ($\mathbf{\Delta}\omega^{\pm}$), and back-donation ($\mathbf{\Delta E_{back-d}}$) were calculated according to the following equation:

$$\boldsymbol{\Delta}\mathrm{E}_{\mathrm{gap}} = \mathrm{E}_{\mathrm{LUMO}} - \mathrm{E}_{\mathrm{HOMO}} \tag{1}$$

$$\boldsymbol{\eta} = \frac{\mathrm{E}_{\mathrm{LUMO}} - \mathrm{E}_{\mathrm{HOMO}}}{2} \tag{2}$$

$$\boldsymbol{\sigma} = \frac{1}{\boldsymbol{\eta}} = \frac{2}{\mathrm{E}_{\mathrm{LUMO}} - \mathrm{E}_{\mathrm{HOMO}}} \tag{3}$$

$$\boldsymbol{\omega} = \frac{\chi^2}{2\boldsymbol{\eta}} \tag{4}$$

$$\boldsymbol{I} = -\mathrm{E}_{\mathrm{HOMO}} \tag{5}$$

$$\boldsymbol{A} = -\mathrm{E}_{\mathrm{LUMO}} \tag{6}$$

$$\boldsymbol{\omega^-} = \frac{(3\boldsymbol{I} + \boldsymbol{A})^2}{16(\boldsymbol{I} - \boldsymbol{A})} \tag{7}$$

$$\boldsymbol{\omega^+} = \frac{(\boldsymbol{I} + 3\boldsymbol{A})^2}{16(\boldsymbol{I} - \boldsymbol{A})} \tag{8}$$

$$\Delta\omega^{\pm} = \left\{\omega^+ - (-\omega^-)\right\} \text{ or } \Delta\omega^{\pm} = \left\{\omega^+ - \left(\frac{1}{\omega^-}\right)\right\} \tag{9}$$

$$\boldsymbol{\Delta}\mathrm{E}_{\mathrm{back-d}} = -\frac{\boldsymbol{\eta}}{4} \tag{10}$$

Furthermore, the local reactivity for both BCT and B_{36} molecules was examined through the Fukui indices according to the following equations [53–55]:

$$\boldsymbol{f_k^+} = \boldsymbol{q_K}(\boldsymbol{N}+1) - \boldsymbol{q_K}(\boldsymbol{N}) \text{(Nucleophilic attack)} \tag{11}$$

$$\boldsymbol{f_k^-} = \boldsymbol{q_K}(\boldsymbol{N}) - \boldsymbol{q_K}(\boldsymbol{N}-1) \text{ (Electrophilic attack)} \tag{12}$$

where $\boldsymbol{q_K}$ is the gross charge of atom k at the molecule and N is the number of electrons. Therefore $\boldsymbol{q_K}(\boldsymbol{N})$, $\boldsymbol{q_K}(\boldsymbol{N}+1)$, and $\boldsymbol{q_K}(\boldsymbol{N}-1)$ are charge values of atom k for neutral, cation, and anion, respectively. Local electrophilicity (ω_k^+, ω_k^-) and local softness (δ_k^+, δ_k^-) indexes are calculated by the following equations:

$$\omega_k^+ = \omega f_k^+ \text{(Nucleophilic attack)} \tag{13}$$

$$\omega_k^- = \omega f_k^- \text{ (Electrophilic attack)} \tag{14}$$

$$\delta_k^+ = \delta f_k^+ \textit{(Nucleophilic attack)} \tag{15}$$

$$\delta_k^+ = \delta f_k^- \textit{ (Electrophilic attack)} \tag{16}$$

The expression used to calculate the adsorption energy is as follows [27–29]:

$$E_{\mathrm{ads}} = \left(E_{[B_{36}@(\mathrm{BCT})_n]} - E_{B_{36}} - nE_{\mathrm{BCT}}\right)/n \tag{17}$$

$\mathrm{E}_{[\mathrm{B}_{36}@(\mathrm{BCT})_n]}$ represents the total energy of the B_{36}@$(\mathrm{BCT})_n$ complex, $\mathrm{E}_{\mathrm{B}_{36}}$ denotes the energy of the isolated B_{36} nanosheet, and $\mathrm{E}_{\mathrm{BCT}}$ stands for the energy of the isolated single BCT molecule. The thermal stability of BCT@B_{36} complex is also examined by conducting the ab-initio molecular dynamic (AIMD) simulations at 300 K and 400 K.

3 Results and discussion

3.1 Structure proprieties of B_{36} and BCT

It has been reported in the literature [56–62] that the interaction between two molecular systems, specifically between an adsorbate and adsorbent surface, is highly dependent on the respective donor and acceptor abilities of the molecules involved. Molecules with high E_{HOMO} values tend to donate electrons to a low E_{LUMO} of suitable acceptor molecule. Charge transfer in molecular systems depends on the energy gap between E_{HOMO} and E_{LUMO}, a larger ΔE_{gap} is indicative of a lower reactivity, while a smaller ΔE_{gap} values is associated with higher reactivity of a chemical species.

The calculated global reactivity descriptors such as highest occupied molecular orbital energy (E_{HOMO}), lowest unoccupied molecular orbital energy (E_{LUMO}), energy gap (ΔE_{gap}), global hardness (η), global softness (σ), global electrophilicity (ω), and back-donations of electrons ($\Delta E_{back\text{-}d}$) are listed in Table 1. Based on the calculated reactivity descriptors, the B_{36} borophene exhibits high reactivity associated with low energy gap (1.881 eV) and high softness values (1.063 eV). DFT calculations revealed also that the B_{36} borophene has the high electrophilicity index (ω) compared to BCT molecule, which means a good acceptor behavior to interact with BCT.

Table 1 Calculated global reactivity descriptors

Descriptors	BCT	B_{36}
E_{HOMO} (eV)	−7.208	−5.732
E_{LUMO} (eV)	−0.829	−3.851
ΔE_{gap}(eV)	6.379	1.881
TE (a.u.)	−2765.997	−893.101
χ	4.018	4.791
η	3.189	0.941
σ	0.314	1.063
ω	2.531	12.204

The frontier molecular orbitals HOMO and LUMO were used to explain and to understand the chemical reactivity of the BCT and B_{36} structures. Optimized BCT and B_{36} electronic structures at B3LYP-D3/def2-TZVPP level of theory associated with their frontier molecular orbitals (HOMO and LUMO) are shown in Fig. 2.

One observation that can be made is that in the BTC structure, the lowest unoccupied molecular orbital (LUMO) was primarily found to be localized on the carbonyl bond (C═O), while the highest occupied molecular orbital (HOMO) is spread out over the entire molecule but has a particularly high concentration on the oxygen atom in the carbonyl group and on the bromo atom. This indicates that these atoms may be able to interact effectively with the B_{36} surface by providing electrons. In contrast, in the B_{36} structure, the electron densities of both the highest occupied molecular orbital (HOMO) and the lowest unoccupied molecular orbital (LUMO) are mainly spread across the surface of the B_{36} molecule, with a significant contribution from the boron atoms on the sides. This suggests that the

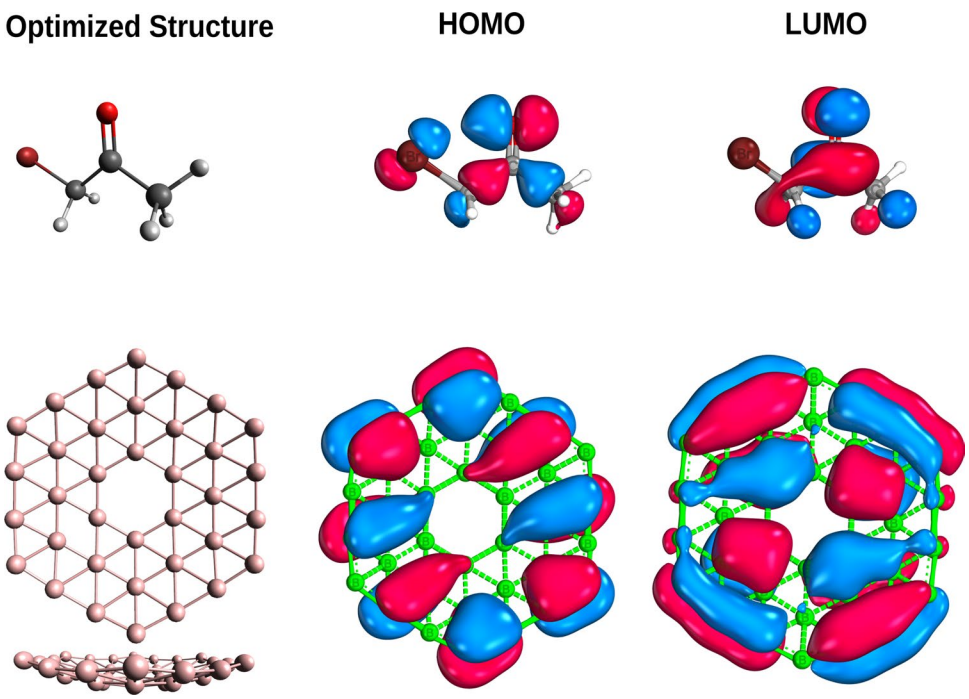

Fig. 2 Optimized structures and frontier molecule orbital density distribution (HOMO and LUMO) of BCT and B_{36}borophene nanosheet obtained at B3LYP/def2-TZVPP level

most reactive sites for both electrophilic and nucleophilic attacks are located in these regions. Furthermore, the molecular electrostatic potential (MEP) analysis corroborates with the results of frontier molecular orbitals suggesting that the most reactive site on the B_{36} borophene are the lateral atoms of B_{36} structure indicated by negative charge (red surface color), although the most reactive site of the BCT molecule is the oxygen atom into the carbonyl group, as shown in Fig. 3.

In addition, the Fukui function was used to analyze the local reactivity of B_{36} and BCT molecules, in order to provide information on the preferential sites for electrophilic and nucleophilic attacks. The calculated condensed Fukui function, local electrophilicity, and local softness of B_{36} and BCT using Hirshfeld atomic charges are summarized in supplementary data Tables S1 and S2 respectively. However, the isosurface Fukui maps of the electrophilic and nucleophilic attacks are shown in Fig. 4, associated with the most high values of calculated Fukui indices f_k^+ (red) and f_k^- (blue). Upon examining the isosurface Fukui maps presented in Fig. 4, it becomes apparent that in the case of BCT, the oxygen and bromo atoms serve as favorable sites for both nucleophilic and electrophilic attacks. Concerning the B_{36} surface, the boron atoms B21, B24, B27, B30, B33, and B36 are identified as preferred sites for nucleophilic attacks, while B27, B28, B29, B30, B33, and B36 atoms are deemed suitable for electrophilic attacks, as illustrated in Fig. 4.

3.2 Adsorption of single BCT molecule on the B_{36} nanosheet

Based on the results of DFT calculations, we have considered and compared three most stable adsorption configurations, as summarized and shown in Fig. 5a–c, the corresponding frontier molecular orbitals HOMO and LUMO are illustrated in Fig. 6.

The BCT molecule can adsorb on the B_{36} borophene nanosheet with the formation of B−O bond at the edge side of the B_{36} borophene associated with an adsorption energy of − 95.08 kj/mol. The B−O bond established between the BCT molecule and the B_{36} nanosheet, with a length of 1.48 Å is slightly shorter than the sum of O−B covalent radii ($r_O^{cov} + r_B^{cov} = 0.66 + 0.84 = 1.50$ Å) [63], and considerably shorter than the van der Waals sum ($r_O^{van} + r_B^{van} = 1.40 + 1.74 = 3.14$ Å) [64], which implies the potential implication of a chemisorption process as a feasible mechanism for inhibition.

On the other hand, the BCT molecule can also interact with B_{36} borophene without formation of any covalent bonds between them. This interaction can occur through two distinct stable complexes: one situated at the concave side (Fig. 5b) with an interaction energy of approximately − 78.16 kj/mol and the other at the convex side with an energy of approximately − 50.07 kj/mol.

The computed distances between the atoms of BCT molecule (C, H, O, and Br atoms) and the closest boron atoms of B_{36} borophene in BCT@B_{36} concave and BCT@B_{36} convex complexes fall within the range of 3.06–3.10 Å. These interactions exhibit lengths that are notably surpassing the sum of the covalent radii of B−O (1.50 Å), B − H (1.15 Å), B−C (1.60 Å), and B−Br (2.04 Å) [63]. Furthermore, these lengths are comparatively longer than the van der Waals sum of the selected atoms B−O (3.14 Å), B − H (2.94 Å), B−C (3.44 Å), and B−Br (3.69 Å) [64]. Consequently, these interactions involve weak attractive forces between the BCT molecule and the B_{36} nanosheet.

The inspection of the frontier molecular orbital distributions including the highest occupied molecular orbital energy (HOMO) and lowest unoccupied molecular orbital energy (LUMO) for the concave and convex BCT@B_{36} complexes shows that the HOMO and LUMO orbitals are entirely localized on the B_{36} borophene. This is in contrast to the edge configuration where the LUMO distribution is

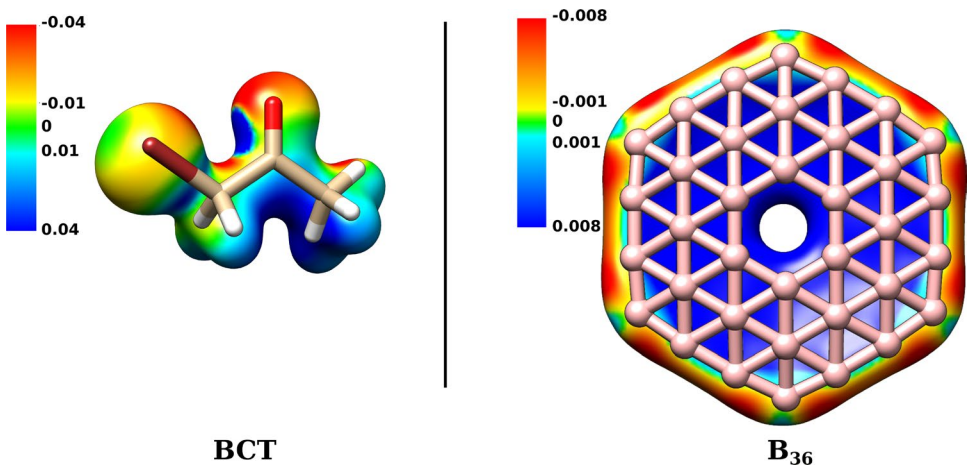

Fig. 3 Molecular electrostatic potential (MEP) maps for both BCT and B_{36} borophene nanosheet

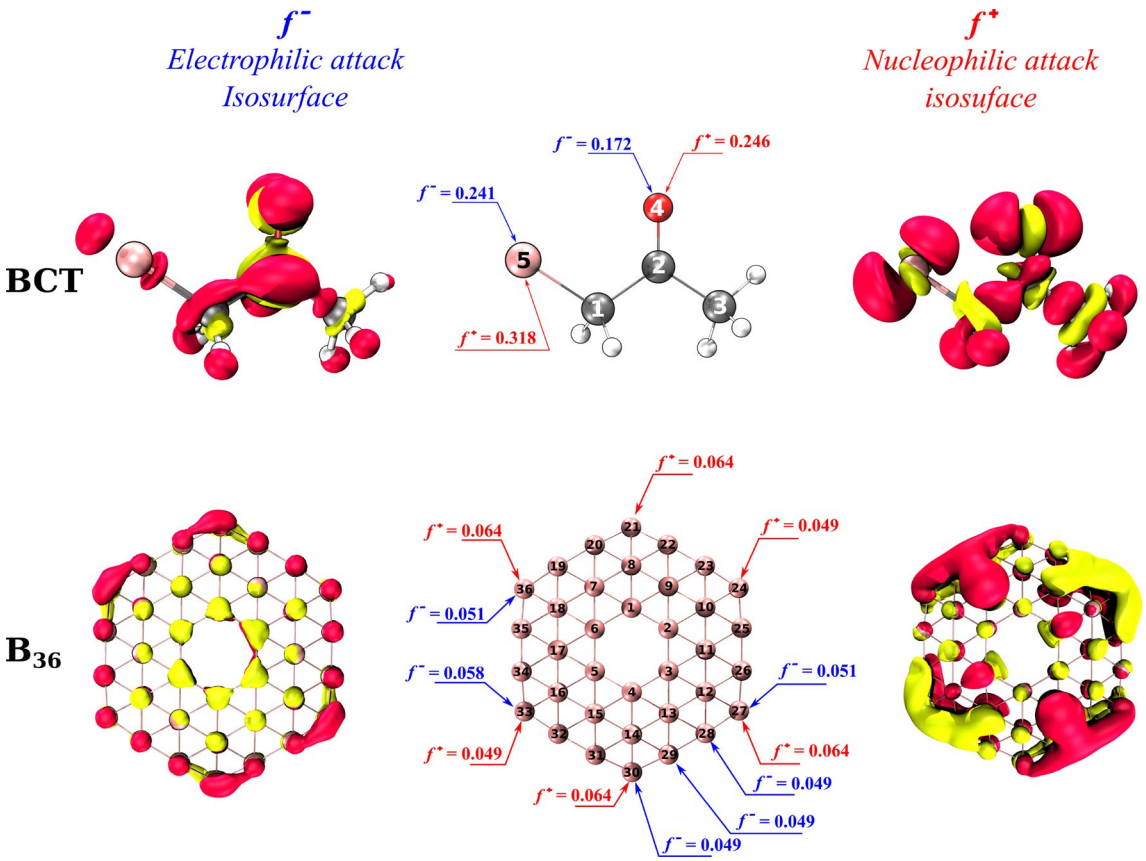

Fig. 4 Isosurface Fukui maps (electrophilic attack f^- (left) and nucleo-philic attack f^+ (right)), and the most high values of calculated Fukui functions f^- and f^+ (center) for both BCT and B_{36}b orophene nanosheet structures

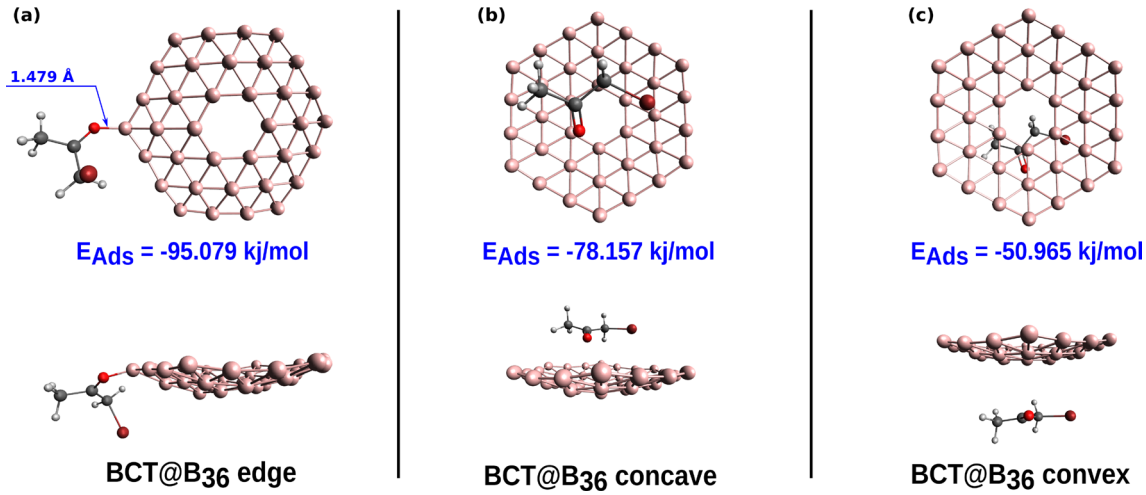

Fig. 5 Optimized geometries of the three most stable complexes; **a** BCT@B_{36} edge, **b** BCT@B_{36} concave, and **c** BCT@B_{36} convex

mainly localized on the BCT molecule, while the HOMO orbital is localized across the entire BCT@B_{36} structure.

Furthermore, the non-covalent interaction analysis based on the reduced density gradient (RDG-NCI) analysis was also carried out to examine and identify the nature of interactions responsible for its exceptional stability in the studied systems, including the intermolecular interactions in the BCT@B_{36} concave and BCT@B_{36} convex complexes.

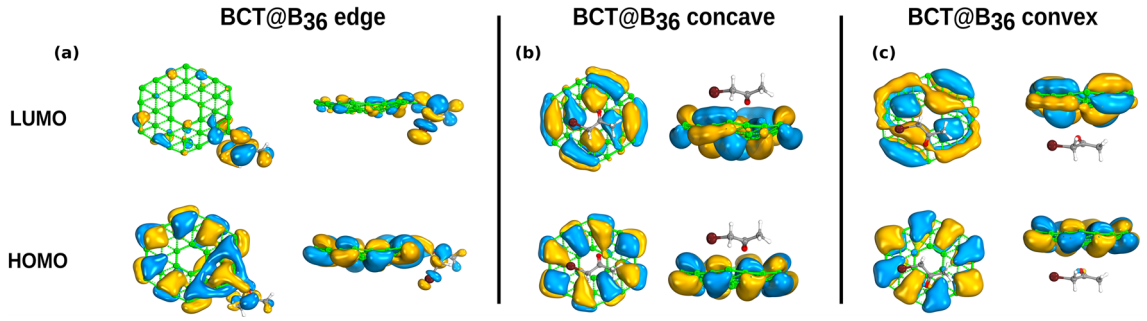

Fig. 6 Frontier molecular orbital distributions (HOMO and LUMO) of the three most stable complexes; **a** BCT@B_{36} edge, **b** BCT@B_{36} concave, and **c** BCT@B_{36} convex

Figure 7 displays the RDG-NCI isosurfaces for the three most stable complexes, namely the edge, concave, and convex configurations (see Fig. 7a–c). The color spectrum varies from blue to red, representing values falling within the range of -0.05 a.u. $< \rho$*sign($\lambda 2$) < 0.05 a.u.

Larger green isosurfaces were noticed between the BCT molecule and the B_{36} nanosheet in the case of the BCT@B_{36} concave and convex complexes (configurations b and c, respectively). These isosurfaces were distinctly characterized by the combination of light green and dark coloration.

The light green area indicates strong interactions being dominated by van der Waals forces. These contacts were observed not only between the oxygen atom of the carbonyl group and the B_{36} surface but also between the bromo atom and the B_{36}, as well as between the bottommost hydrogen atoms of the methyl groups and the B_{36} surface. The 2D RDG scatter plots further confirm the existence of these weak interactions within the region of $\lambda 2(\rho)$ from -0.002 to -0.012 atomic units (a.u.), as illustrated in Fig. 7b and c. We can also observed a dark green area in the isosurface of BCT@B_{36} concave and convex complexes between carbon atom of BCT molecule and B_{36} surface, corresponding to the ranges between 0.00 and 0.01 a.u., as shown in the 2D scatter plot (Fig. 7b and c), due to the week interaction of van der Waals force.

On the other hand, in the most stable configuration BCT@B_{36} edge (configuration a), we find that not only the formation of covalent B−O bond which stabilized the complex formed, but also a van der Waals type interaction was formed between bromo atom of BCT molecule and the

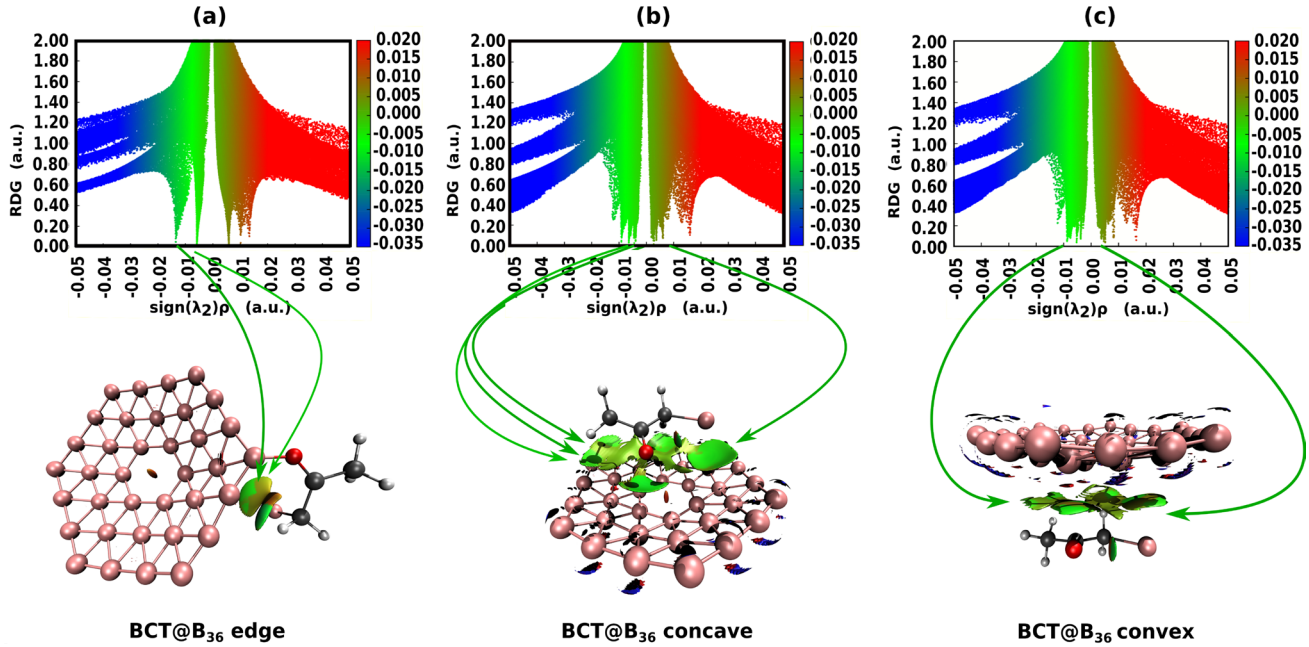

Fig. 7 The non-covalent interaction-reduced density gradient analysis (NCI-RDG); **a** BCT@B_{36} edge, **b** BCT@B_{36} concave, and **c** BCT@B_{36} convex

side boron B atom of B_{36} surface. This observation is effectively depicted in Fig. 7a, where a green isosurface is visible between the bromo atom of the BCT molecule and the boron B atom of B_{36}. Additionally, in the 2D RDG graph, this interaction is evident at approximately 0.005 and 0.015 u.a., further affirming the presence of van der Waals forces.

Additionally, we explored the charge redistribution after the interaction of the BCT molecule with the B_{36} nanosheet via the charge density difference (CDD) calculations. Figure 8 displays the charge density difference (CDD) plots for the most stable configurations of the interaction between the BCT molecule and B_{36} nanosheet. These plots utilize an isosurface value of 0.002 e/Å^3, where the red cardinal regions indicate charge depletion (electron loss), while the yellow regions show charge buildup (electron enrichment). As can be visually observed in Fig. 8, the formation of direct B−O bond is clearly shown by the most significant charge redistributions. Furthermore, it has been observed that less significant charge redistributions occur between the bromo atom of the BCT molecule and the boron B atom of the B_{36} nanosheet, leading to an increase in binding energy.

The analysis of charge density difference (CDD) for BCT@B_{36} concave and convex configurations (refer to Fig. 8b and c) showed a similar behavior and indicates the presence of an electrostatic interaction between the oxygen atom of the carbonyl group in the BCT molecule and the B_{36} nanosheet. This is evident from the observed charge redistribution around the C=O group and the smaller yellow regions indicating charge accumulation on the borophene surface, all without the formation of covalent bonds.

Based on the calculated molecular descriptors (Table 2), the interaction between the BCT molecule and the B_{36} nanosheet leads to a shift in the HOMO energy level toward higher energies. Specifically, for the BCT@B_{36} edge complex, it shifts to − 5.17 eV, for the BCT@B_{36} concave complex, it shifts to − 5.61 eV, and for the BCT@B_{36} convex complex, it shifts to − 5.64 eV. However, in contrast to both the BCT@B_{36} concave and BCT@B_{36} convex complexes, where the energy of the LUMO shifts to higher energy levels, the LUMO orbitals in the BCT@B_{36} edge complex exhibit a shift toward lower energy levels, leading to a reduction in the energy gap (ΔE_{gap}).

Analysis of the DOS spectral results reveals also that the BCT@B_{36} edge configuration is more affected after interaction between BCT and B_{36} compared to its two analogs (BCT@B_{36} concave and BCT@B_{36} convex complexes), as shown in Fig. 9. The reduction in the HOMO–LUMO energy gap follows a descending order: BCT@B_{36} convex (1.89 eV) > BCT@B_{36} concave (1.83 eV) > BCT@B_{36} edge (1.17 eV). This substantial decrease in the energy gap implies a significant alteration in the electronic conductivity of the B_{36} nanosheet upon interaction with the BCT molecule. These beneficial changes have the potential to be applied in the development of molecular sensors.

3.3 Ab-initio molecular dynamic (AIMD) simulations of adsorption

The ab-initio molecular dynamic (AIMD) simulations were executed using the ORCA software (version 5.0.4) [38, 65].

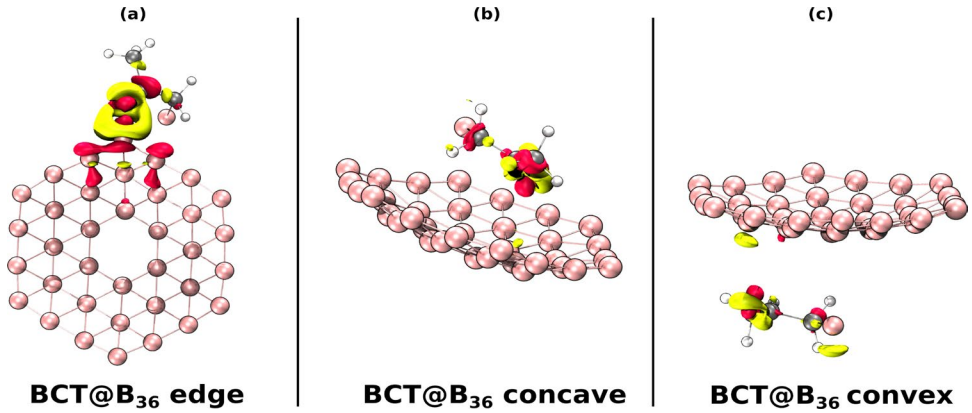

Fig. 8 The charge density difference (CDD) maps of the three most stable complexes; **a** BCT@B_{36} edge, **b** BCT@B_{36} concave, and **c** BCT@B_{36} convex

Table 2 Descriptors BCT@B_{36} edge, BCT@B_{36} concave, and BCT@B_{36} convex

Descriptors	B_{36}	BCT@B_{36}edge	BCT@B_{36}concave	BCT@B_{36} convex
E_{HOMO} (eV)	− 5.73	− 5.17	− 5.61	− 5.64
E_{LUMO} (eV)	− 3.85	− 4.00	− 3.78	− 3.75
ΔE_{gap}(eV)	1.88	1.17	1.83	1.89
μ (Debye)	2.43	11.62	1.77	4.82
TE (a.u.)	− 893.10	− 3659.13	− 3659.13	− 3659.12

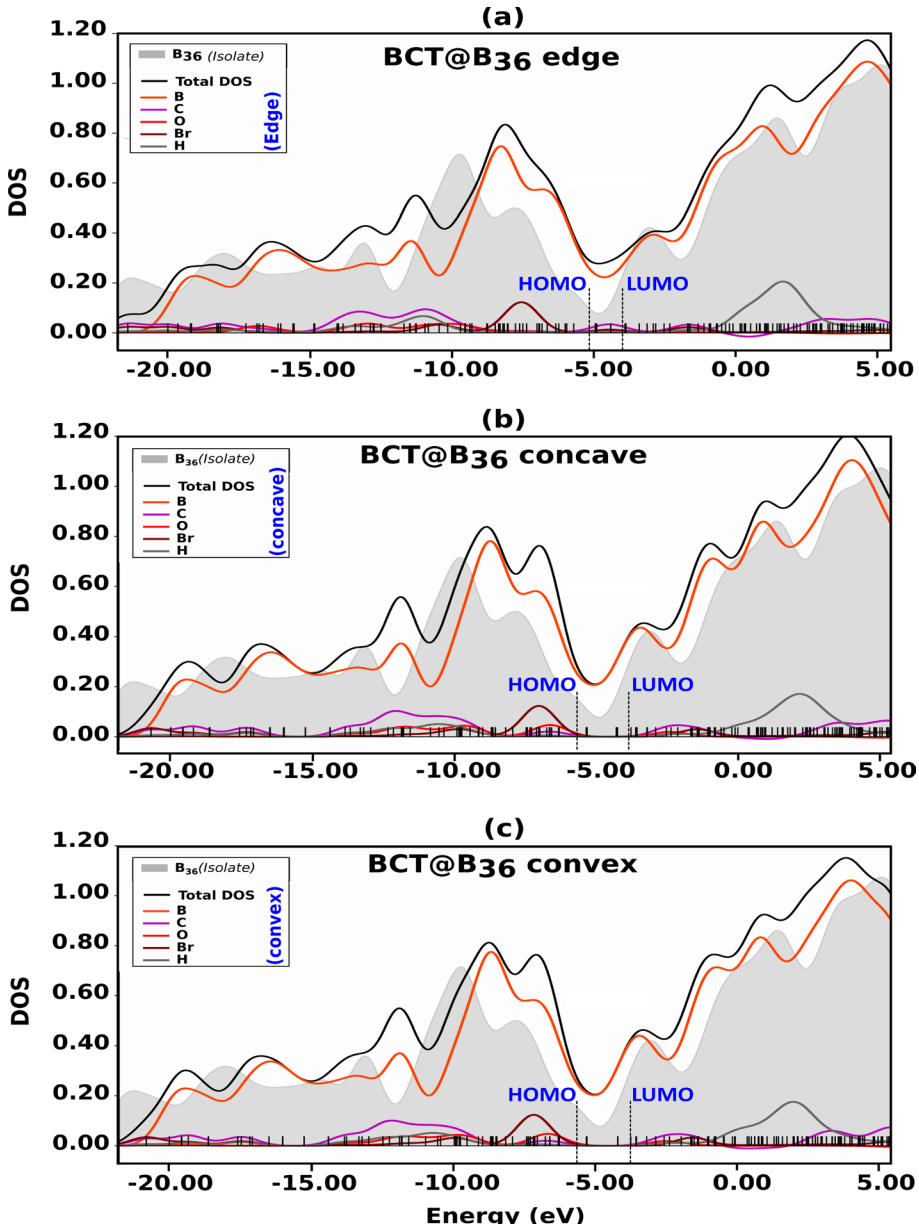

Fig. 9 The density of state (DOS) of the three most stable complexes; **a** BCT@B_{36} edge, **b** BCT@B_{36} concave, and **c** BCT@B_{36} convex

For all systems, a time step of 1.0 fs was employed, and the temperature was set at T = 300 K.

We explore the thermal stability and predict the behavior of both concave and convex BCT@B_{36} complexes using AIMD simulations at temperatures of 300 K and 400 K. The computational results from AIMD simulations for both types of complexes at the 300 K and 400 K temperatures are depicted in Fig. 10.

As illustrated in Fig. 10, the root mean square deviation (RMSD) curves exhibit consistent periodic fluctuations for both concave and convex BCT@B_{36} complexes at 300 K and 400 K. The comparison between the two RMSD of BCT@B_{36} concave and BCT@B_{36} convex clearly indicates that BCT@B_{36} convex is the more thermally stable configuration at 300 K. Upon comparing the two RMSD curves at 300 K and 400 K for BCT@B_{36} complexes, it becomes evident that the higher the simulation temperature, the more significant the geometric fluctuation attributed to thermal motion.

3.4 Adsorption of multiple BCT molecules on the B_{36} nanosheet

We have investigated the impact of concentration by examining the adsorption of one to six bromoacetone (BCT) molecules on borophene B_{36} nanosheet. With this aim in mind, we chose the most stable complex featuring a singly edge-adsorbed BCT. Subsequently, additional BCT molecules were systematically introduced, progressing incrementally at

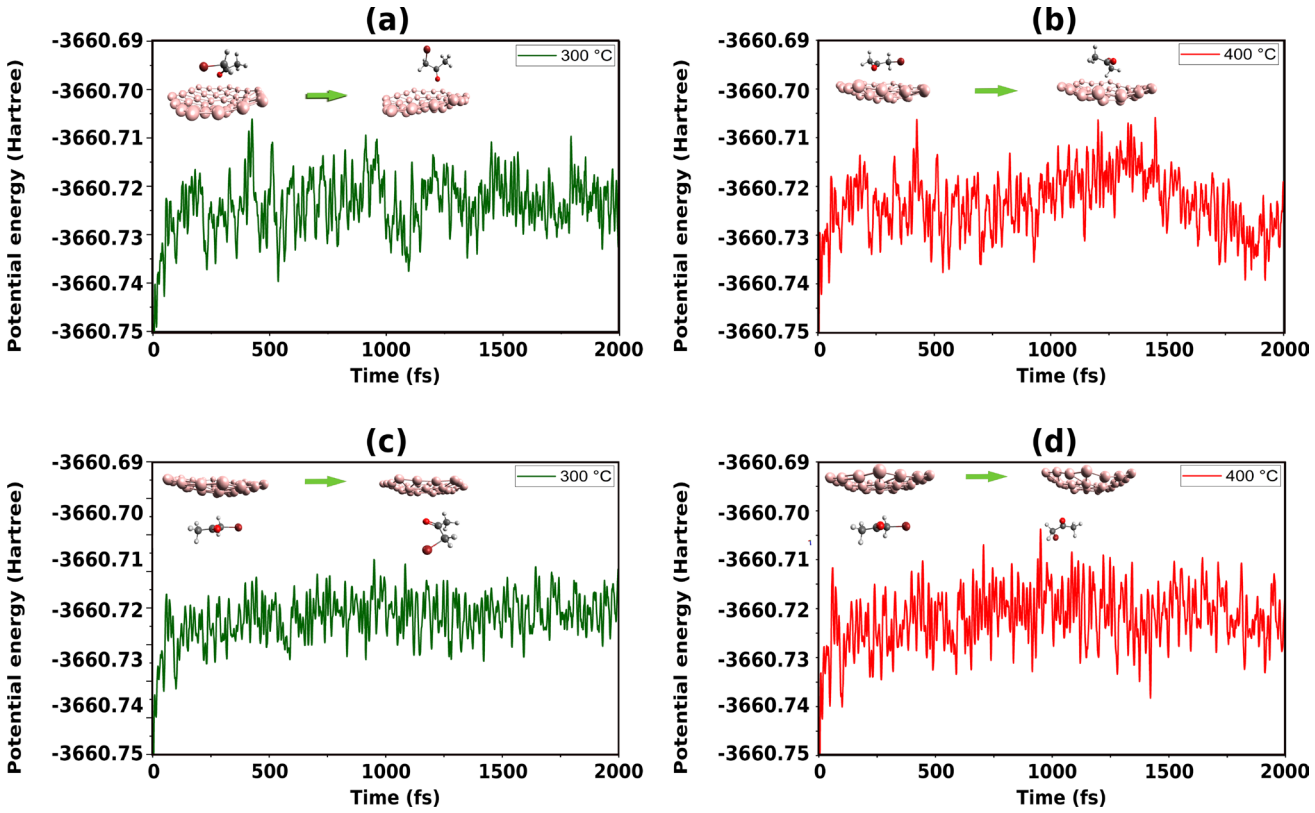

Fig. 10 RMSD of the potential energy: **a** BCT@B_{36} concave at 300 K, **b** BCT@B_{36} concave at 400 K, **c** BCT@B_{36} convex at 300 K, and **d** BCT@B_{36} convex at 400 K

the edge, concave, and convex sides, with a primary emphasis on edge-side adsorption.

We conducted a reoptimization procedure for each configuration using the B3LYP-D3BJ-SMD/Def2-SVP level of theory, with RIJCOSX approximation. Subsequently, for each newly optimized complex, an exploration of various possible configurations was compared.

Therefore, Figs. 11 and 12 depict the most stable configurations, while Table 3 provides detailed information on the adsorption energies of multiple BCT molecules on the B_{36} nanosheet.

Based on DFT calculation results (Table 3, Figs. 11 and 12), B_{36} borophene nanosheet has the capacity to absorb more than a single BCT molecule. It is worth noting that B_{36} has the capability to capture up to five BCT molecules (an exothermic process), facilitated by spontaneous attachment corroborated by the negative adsorption energy, as illustrated in Table 3.

Contrarily, in the case of the adsorption of six BCT molecules on B_{36} borophene, the calculation results yield a positive value for the adsorption energy (an endothermic process), except for the configuration 4-AC-EDGE + 1AC-CONCAVE + 1AC-CONVEX, which exhibits a negative adsorption energy, suggesting a strong interaction between the BCT and B_{36} borophene molecules. The calculated adsorption energies at the B97-D3(BJ)/def2-SVP level (Table 3) reveal that the most stable complexes (2-EDGE, 3-EDGE, 4-EDGE, and 5-EDGE) feature the adsorption of BCT molecules at the edge sites of the B_{36} nanosheet.

We also note that in configurations involving four, five, and six molecules of BCT adsorbed on B_{36} borophene, certain BCT molecules underwent dissociation reactions into acetonyl radicals and bromine atom fragments during the adsorption process on B_{36} borophene, as illustrated in Fig. 12 (4-EDGE (a), 5-EDGE (a–d), and 6-EDGE (b and c)).

Nevertheless, in the 5-EDGE + 1-CONCAVE configuration, the BCT molecule formed a covalent B−O bond with B_{36} borophene, leading to a bond length of 1.43 Å. This measured distance is marginally less than the combined covalent radii of O−B ($r_O^{cov} + r_B^{cov} = 0.66 + 0.84 = 1.50$ Å) [63], suggesting the plausibility of a chemisorption process as the mechanism for adsorption.

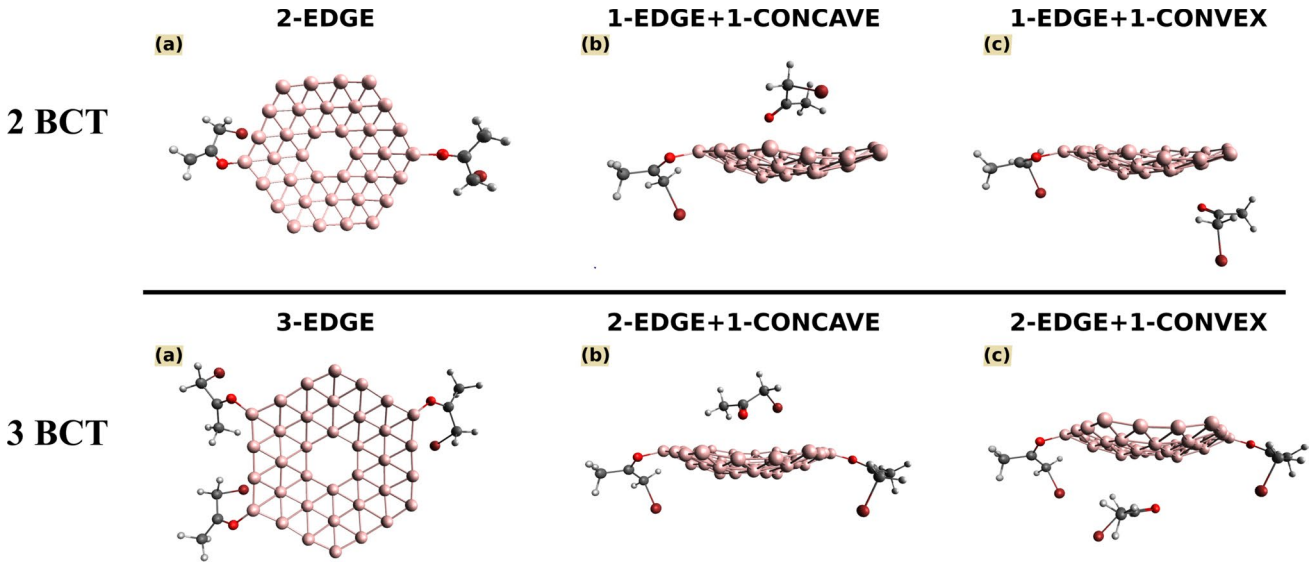

Fig. 11 Optimized geometry structures for studied complexes with two (2 BCT) and three (3 BCT) adsorbed BCT molecules

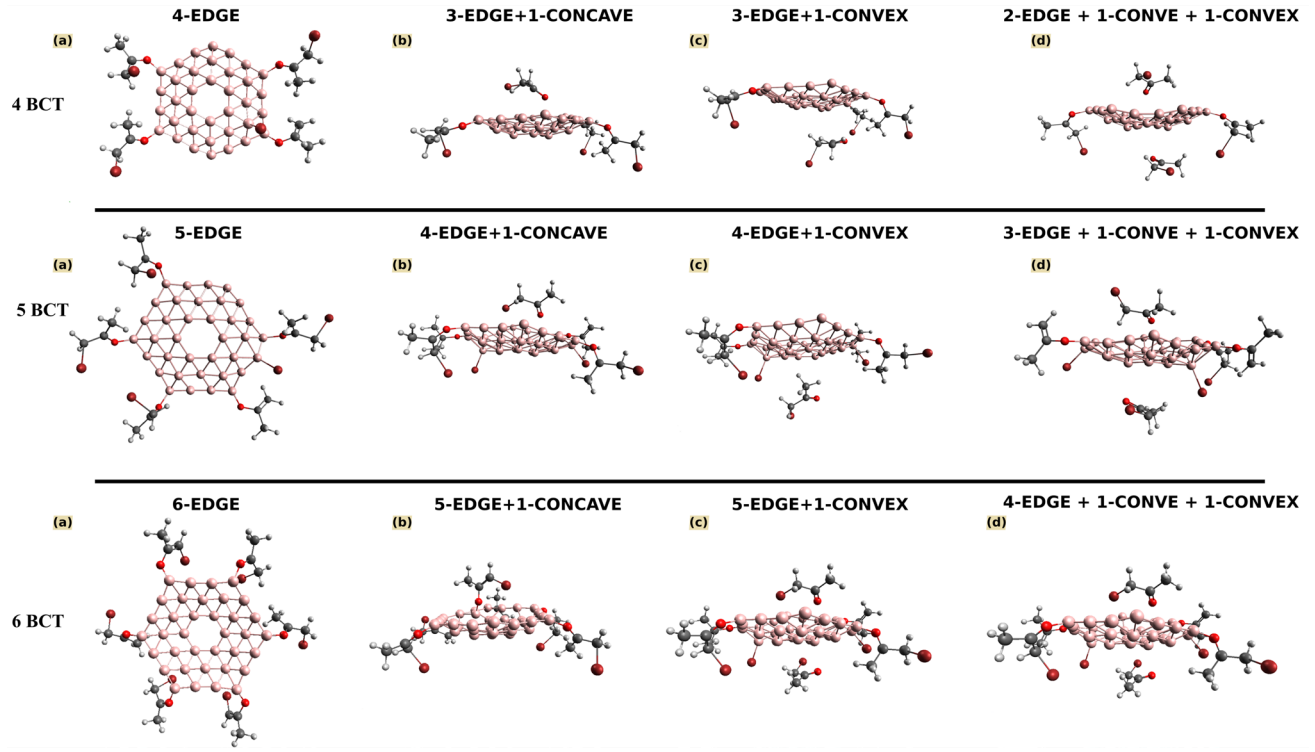

Fig. 12 Optimized geometry structures for studied complexes with four (4 BCT), five (5 BCT) and six (6 BCT) adsorbed BCT molecules

4 Conclusion

In summary, a computational study has been performed on the B_{36} borophene nanosheets as sensors for detecting bromoacetone (BCT) molecule. The main conclusions that can be drawn from this study are the following:

- The B_{36} borophene nanosheets effectively senses the BCT molecule, adsorbing up to five BCT molecules via an exothermic process.

Table 3 Adsorption energies of multiple BCT molecules on the B_{36} nanosheet

Num. Molecules	Configurations	E_{ads}
2 BCT	2-EDGE	− 215,178,833
	1-EDGE + 1-CONCAVE	− 201,875,533
	1-EDGE + 1-CONVEX	− 163,551,717
3 BCT	3-EDGE	− 198,956,479
	2-EDGE + 1-CONCAVE	− 185,218,901
	2-EDGE + 1-CONVEX	− 180424499
4 BCT	4-EDGE	− 323,081,416
	3-EDGE + 1-CONCAVE	− 182,815,627
	3-EDGE + 1-CONVEX	− 171,630,389
	2-EDGE + 1-CONVEX + 1-CONVEX	− 181,244,258
5 BCT	5-EDGE	− 384,138,118
	4-EDGE + 1-CONCAVE	− 379,672,921
	4-EDGE + 1-CONVEX	− 368,178,887
	3-EDGE + 1-CONVEX + 1-CONVEX	− 370708528
6 BCT	6-EDGE	102,824,311
	5-EDGE + 1-CONCAVE	103,715,347
	5-EDGE + 1-CONVEX	942,436,237
	4-AC-EDGE + 1AC-CONCAVE + 1AC-CONVEX	− 338,401,418

- DFT calculations revealed that the most stable configurations among the complexes are BCT@B_{36} edge, BCT@B_{36} concave, and BCT@B_{36} convex.
- The BCT molecule can adsorb through the formation of B−O bond, involving the oxygen atom of the carbonyl group in BCT and the edge boron atoms of B_{36} borophene, indicating a chemisorption process.
- The BCT molecule can also physio-adsorb on both the concave and convex sides of B_{36} borophene nanosheets, facilitated by van der Waals interactions.
- The results of ab-initio molecular dynamics (AIMDs) validate the thermal stability of both the BCT@B_{36} concave and BCT@B_{36} convex complexes at temperatures of 300 K and 400 K.

Supplementary Information The online version contains supplementary material available at https://doi.org/10.1007/s10825-024-02192-3.

Acknowledgements The authors express their gratitude to the University of Constantine 1 for its support in the completion of this work.

Author contributions **M.T.**—Investigation and ORCA software. **H.A.**—Administration of projects, reviewing and editing, and validating. **S.B.**—Reviewed the manuscript. **F.B.**—Investigation, multiwfn software, and RDG analysis. **S.M.**—Investigation, multiwfn software, and CDD analysis. **M.D.**—Writing the manuscript. **A. B.**—Writing the manuscript.

Funding The authors assert the absence of any funding sources.

Data availability Not applicable.

Declarations

Conflict of interest The authors declare no competing interests.

Code availability Not applicable.

References

1. Deng, J., Guo, J., Zhou, X., Zhou, P., Fu, X., Zhang, W., Lin, K.: Hazardous substances in indoor dust emitted from waste TV recycling facility. Environ. Sci. Pollut. Res. **21**(12), 7656–7667 (2014)
2. Deng, J., Guo, J., Zhou, X., Zhou, P., Fu, X., Zhang, W., Lin, K.: Hazardous substances in indoor dust emitted from waste TV recycling facility. Environ. Sci. Pollut. Res. **21**, 7656–7667 (2014)
3. McCunney, R.J.: Health effects of work at waste water treatment plants: a review of the literature with guidelines for medical surveillance. Am. J. Ind. Med. **9**, 271–279 (1986)
4. Chandiramouli, R., Nagarajan, V.: Transport studies of CeO_2 molecular device and adsorption behavior of CO on CeO_2 device: a first-principles investigation. J. Comput. Electron. **16**, 316–324 (2017)
5. Golding, J.: Unnatural constituents of breast milk-medication, lifestyle, pollutants, viruses. Early. hum. dev. **49**, S29–S43 (1997)
6. DeCoste, J.B., Peterson, G.W.: Metal-organic frameworks for air purification of toxic chemicals. Chem. Rev. **114**, 5695–5727 (2014)
7. Gopakumar, D.A., Pasquini, D., Henrique, M.A., de Morais, L.C., Grohens, Y., Thomas, S.: Meldrum's acid modified cellulose nanofiber-based polyvinylidene fluoride microfiltration membrane for dye water treatment and nanoparticle removal. ACS. Sustain. Chem. Eng. **5**, 2026–2033 (2017)
8. Lyu, Y., Brusseau, M.L., Chen, W., Yan, N., Fu, X., Lin, X.: Adsorption of PFOA at the air-water interface during transport in unsaturated porous media. Environ. Sci. Technol. **52**, 7745–7753 (2018)
9. Saravanan, A., Senthil, K.P., Jeevanantham, S., Karishma, S., Tajsabreen, B., Yaashikaa, P.R., Reshma, B.: Effective water/wastewater treatment methodologies for toxic pollutants removal: processes and applications towards sustainable development. Chemosphere **280**, 130595 (2021)
10. Bhuvaneswari, R., Nagarajan, V., Chandiramouli, R.: First-principles analysis of the detection of amine vapors using an antimonene electroresistive molecular device. J. Comput. Electron. **18**, 779–790 (2019)
11. Srivastava, V.C., Mall, I.D., Mishra, I.M.: Adsorption of toxic metal ions onto activated carbon. Chem. Eng. Process. **47**, 1269–1280 (2008)
12. Tang, Z.K., Nozue, Y., Goto, T.: Quantum size effect on the excited state of HgI_2, PbI_2 and BiI_3 clusters and molecules in zeolite LTA. J. Phys. Soc. Jpn. **61**, 2943 (1992)
13. Sigot, L., Ducom, G., Germain, P.: Adsorption of octamethylcyclotetrasiloxane (D4) on silica gel (SG): retention mechanism. Microporous Mesoporous Mater. **213**, 118–124 (2015)
14. Besghaier, S., Cecilia, J.A., Chouikhi, N., Vilarrasa-García, E., Rodríguez-Castellón, E., Chlendi, M., Bagane, M.: Glyphosate adsorption onto porous clay heterostructure (PCH): kinetic and thermodynamic studies. Braz. J. Chem. Eng. **39**, 903–917 (2022)
15. Vinuth, M., Naik, H.S.B., Mahadevaswamy, M.M., Prabhakara, M.C.: Environmentally benign Fe(III)–montmorillonite

for rapid adsorption of methylene blue dye in aqueous medium under ambient conditions. Fash. Text. **4**, 8 (2017)
16. Scholtzová, E., Jankovič, L., Tunega, D.: Montmorillonite as an anti-tuberculosis rifampicin drug carrier: DFT and experimental study. Clays Clay Miner. **71**, 229–241 (2023)
17. Jin-feng, P., Wu, R., Chen, X.: Preparation of benzene adsorption materials using waste activated alumina. J. Shanghai Jiaotong Univ. Sci. **17**, 373–376 (2012)
18. Manjare, S.D., Ghoshal, A.K.: Comparison of adsorption of ethyl acetate on activated carbon and molecular sieves 5A and 13X. J. Chem. Eng. Data **51**, 1185–1189 (2006)
19. Bardi, N., Giannakopoulou, T., Vavouliotis, A., Trapalis, C.: Electrodeposited films of graphene, carbon nanotubes, and their mixtures for supercapacitor applications. ACS. Appl. Nano. Mater. **3**, 10003–10013 (2020)
20. Snehha, P., Nagarajan, V., Chandiramouli, R.: Germanene nanotube electroresistive molecular device for detection of NO_2 and SO_2 gas molecules: a first-principles investigation. J. Comput. Electron. **18**, 308–318 (2019)
21. Kootenaei, S.A., Ansari, G.: B36 borophene as an electronic sensor for formaldehyde: quantum chemical analysis. Phys. Lett. A **380**, 2664–2668 (2016)
22. Mohsenpour, Z., Shakerzadeh, E., Zare, M.: Quantum chemical description of formaldehyde (HCHO), acetaldehyde (CH_3CHO) and propanal (CH_3CH_2CHO) pollutants adsorption behaviors onto the bowl-shaped B36 nanosheet. Adsorption **23**, 1041–1053 (2017)
23. Valadbeigi, Y., Farrokhpour, H., Tabrizchi, M.: Adsorption of small gas molecules on B_{36} nanocluster. J. Chem. Sci. **127**, 2029–2038 (2015)
24. Rostami, Z., Soleymanabadi, H.: N–H bond cleavage of ammonia on graphene-like B36 borophene: DFT studies. J. Mol. Model. **22**, 70 (2016)
25. Omidvar, A.: Borophene: a novel boron sheet with a hexagonal vacancy offering high sensitivity for hydrogen cyanide detection. Comput. Theor. Chem. **1115**, 179–184 (2017)
26. Rastgou, A., Soleymanabadi, H., Bodaghi, A.: DNA sequencing by borophene nanosheet via an electronic response: a theoretical study. Microelectron. Eng. **169**, 9–15 (2017)
27. Li, W., Zhao, T.: Borophene as an carrier for mercaptopurine drug: electronic study via density-functional theory computations. J. Mol. Model. **29**, 325 (2023)
28. Arabieh, M., Azar, Y.T., Sepehrian, H., Fasihi, J.: DFT exploration of adsorptive performances of borophene to small sulfur-containing gases. J. Mol. Model. **28**, 146 (2022)
29. Allal, H., Belhocine, Y., Rahali, S., Damous, M., Ammouchi, N.: Structural, electronic, and energetic investigations of acrolein adsorption on B36 borophene nanosheet: a dispersion-corrected DFT insight. J. Mol. Model. **26**, 128 (2020)
30. Damous, M., Allal, H., Belhocine, Y., Maza, S., Merazig, H.: Quantum chemical exploration on the inhibition performance of indole and some of its derivatives against copper corrosion. J. Mol. Liq. **340**, 117136 (2021)
31. Bousba, S., Allal, H., Damous, M., Maza, S.: Computational DFT analysis and molecular modeling on imidazole derivatives used as corrosion inhibitors for aluminum in acidic media. Comput. Theor. Chem. **1225**, 114168 (2023)
32. Petrushenko, I.K., Ivanov, N.A., Petrushenko, K.B.: Theoretical investigation of carbon dioxide adsorption on Li+-decorated nanoflakes. Molecules **26**, 7688 (2021)
33. Liu, J., Xu, X., Anantram, M.P.: Role of inelastic electron–phonon scattering in electron transport through ultra-scaled amorphous phase change material nanostructures. J. Comput. Electron. **13**, 620–626 (2014)
34. Böselt, L., Thürlemann, M., Riniker, S.: Machine learning in QM/MM molecular dynamics simulations of condensed-phase systems. J. Chem. Theory Comput. **17**, 2641–2658 (2021)
35. Meng, S., Fu, X., Jiang, L., Shi, L., Wang, X., Liu, X., Wang, J.: Theoretical calculations and experiments on the thermal properties of fluorinated graphene and its effects on the thermal decomposition of nitrate esters. Nanomaterials **12**, 621 (2022)
36. Szinicz, L.: History of chemical and biological warfare agents. Toxicology **214**, 167–181 (2005)
37. Heyl, M., McGuire, R.: Analytical chemistry associated with the destruction of chemical weapons. Springer, Dordrecht (1997)
38. Neese, F.: The ORCA program system. WIREs Comput. Mol. Sci. **2**, 73–78 (2012)
39. Becke, A.D.: Density-functional thermochemistry. III. The role of exact exchange. J. Chem. Phys. **98**, 5648–5652 (1993)
40. Weigend, F., Ahlrichs, R.: Balanced basis sets of split valence, triple zeta valence and quadruple zeta valence quality for H to Rn: design and assessment of accuracy. Phys. Chem. Chem. Phys. **7**, 3297 (2005)
41. Head-Gordon, M., Rico, R.J., Oumi, M., Lee, T.J.: A doubles correction to electronic excited states from configuration interaction in the space of single substitutions. Chem. Phys. Lett. **219**, 21–29 (1994)
42. Najibi, A., Goerigk, L.: The nonlocal kernel in van der Waals density functionals as an additive correction: an extensive analysis with special emphasis on the B97M-V and ωB97M-V approaches. J. Chem. Theory Comput. **14**, 5725–5738 (2018)
43. Chan, B., Dawson, W., Nakajima, T.: Searching for a reliable density functional for molecule–environment interactions, found B97M-V/def2-mTZVP. J. Phys. Chem. A **126**, 2397–2406 (2022)
44. Ehlert, S., Huniar, U., Ning, J., Furness, J.W., Sun, J., Kaplan, A.D., Perdew, J.P., Brandenburg, J.G.: r2SCAN-D4: dispersion corrected meta-generalized gradient approximation for general chemical applications. J. Chem. Phys. **154**, 061101 (2021)
45. Furness, J.W., Kaplan, A.D., Ning, J., Perdew, J.P., Sun, J.: Accurate and numerically efficient r 2 SCAN meta-generalized gradient approximation. J. Phys. Chem. Lett. **11**, 8208–8215 (2020)
46. Palm, W.U., Schmidt, N., Stahn, M., Grimme, S.: A kinetic study of the photolysis of sulfamethoxazole with special emphasis on the photoisomer. Photochem. Photobiol. Sci. **22**, 615–630 (2022)
47. Bursch, M., Neugebauer, H., Ehlert, S., Grimme, S.: Dispersion corrected r2SCAN based global hybrid functionals: r2SCANh, r2SCAN0, and r2SCAN50. J. Chem. Phys. **156**, 134105 (2022)
48. Kruse, H., Grimme, S.: A geometrical correction for the inter- and intra-molecular basis set superposition error in Hartree-Fock and density functional theory calculations for large systems. J. Chem. Phys. **136**, 154101 (2012)
49. Leboeuf, M., Köster, A.M., Jug, K., Salahub, D.R.: Topological analysis of the molecular electrostatic potential. J. Chem. Phys. **111**, 4893–4905 (1999)
50. Goddard, T.D., Huang, C.C., Ferrin, T.E.: Visualizing density maps with UCSF Chimera. J. Struct. Biol. **157**, 281–287 (2007)
51. Lu, T., Chen, F.: Multiwfn: a multifunctional wavefunction analyzer. J. Comput. Chem. **33**, 580–592 (2012)
52. Hsin, J., Arkhipov, A., Yin, Y., Stone, J.E., Schulten, K.: Using VMD: an introductory tutorial. Curr. Protoc. Bioinform. **24**(1), 5–7 (2008)
53. Korchowiec, J., Gerwens, H., Jug, K.: Relaxed Fukui function indices and their application to chemical reactivity problems. Chem. Phys. Lett. **222**, 58–64 (1994)
54. Kinkar, R.R., Hirao, K., Pal, S.: On non-negativity of Fukui function indices II. J. Chem. Phys. **113**, 1372–1379 (2000)
55. Allal, H., Nemdili, H., Zerizer, M.A., Zouchoune, B.: Molecular structures, chemical descriptors, and pancreatic lipase (1LPB) inhibition by natural products: a DFT investigation and molecular docking prediction. Struct. Chem. **35**(1), 223–239 (2023)

56. Sakki, B., Said, M.E., Mezhoud, B.: Experimental and theoretical study on corrosion inhibition of pyridinium salts derivatives for API 5L Gr.B steel in acidic media. J. Adhes. Sci. Technol. **36**, 2245–2268 (2022)
57. Bouasla, S., Sobhi, C., Allal, H., Mecibah, W., Cherifi, M., Bougdah, I.: Synthesis, antioxidant and dft study of some 4-methyl-2h- chromen-2-one derivatives. Rev. Roum. Chim. **66**, 653–660 (2021)
58. Ammouchi, N., Allal, H., Zouaoui, E., Dob, K., Zouied, D., Bououdina, B.: Extracts of *Ruta chalepensis* as green corrosion inhibitor for copper CDA 110 in 3% NaCl medium: experimental and theoretical studies. Anal. Bioanal. Electrochem. **11**, 830–850 (2019)
59. Kaur, D., Sharma, R., Aulakh, D.: The hydrogen bond donor and acceptor ability of thioformic acid. Struct. Chem. **22**, 1015–1030 (2011)
60. Chopra, N., Kaur, D., Chopra, G.: Hydrogen bonded complexes of oxazole family: electronic structure, stability, and reactivity aspects. Struct. Chem. **29**, 341–357 (2018)
61. Ajmal, M., Ali, U., Javed, A., Tariq, A., Arif, Z., Iqbal, J., Shoaib, M., Ahmed, T.: Designing indaceno thiophene–based three new molecules containing non-fullerene acceptors as strong electron withdrawing groups with DFT approaches. J. Mol. Model. **25**, 311 (2019)
62. El-Shishtawy, R.M., Asiri, A.M., Aziz, S.G., Elroby, S.A.K.: Molecular design of donor-acceptor dyes for efficient dye-sensitized solar cells I: a DFT study. J. Mol. Model. **20**, 2241 (2014)
63. Cordero, B., Gómez, V., Platero-Prats, A.E., Reves, M., Echeverría, J., Cremades, E., Barragán, F., Alvarez, S.: Covalent radii revisited. Dalton Trans. (2008). https://doi.org/10.1039/B801115J
64. Batsanov, S.S.: Van der Waals radii of Elements. Inorg. Mater. **37**, 871–885 (2001)
65. Brehm, M.: ORCA 5.0 Molecular dynamics module. (2021)